Received: 14 November 2018 | Revised: 7 February 2019 | Accepted: 12 March 2019

DOI: 10.4218/etrij.2018-0582

ORIGINAL ARTICLE

WILEY ETRI Journal

Design and control of a permanent magnet spherical wheel motor

Junbo Park | **Minki Kim** | **Hyun Gyu Jang** | **Dong Yun Jung** | **Jong Moon Park**

ICT Materials & Components Research Laboratory, Electronics and Telecommunications Research Institute, Daejeon, Rep. of Korea

Correspondance
Junbo Park, ICT Materials & Components Research Laboratory, Electronics and Telecommunications Research Institute, Daejeon, Rep. of Korea.
Email: jp723@etri.re.kr

Funding information
This research was supported by an Institute for Information & Communications Technology Promotion (IITP) grant funded by the Korean government (MSIT) (No. 2017-0-00044, Development of Shape/Function-controllable ICT Convergent Materials/Components for Next-generation Mobility).

We present a permanent magnet–based spherical wheel motor that can be used in omnidirectional mobility applications. The proposed motor consists of a ball-shaped rotor with a magnetic dipole and a hemispherical shell with circumferential air-core coils attached to the outer surface acting as a stator. Based on the rotational symmetry of the rotor poles and stator coils, we are able to model the rotor poles and stator coils as dipoles. A simple physical model constructed based on a torque model enables fast numerical simulations of motor dynamics. Based on these numerical simulations, we test various control schemes that enable constant-speed rotation along arbitrary axes with small rotational attitude error. Torque analysis reveals that the back electromotive force induced in the coils can be used to construct a control scheme that achieves the desired results. Numerical simulations of trajectories confirm that even without explicit methods for correcting the rotational attitude error, it is possible to drive the motor with a low attitude error (<5°) using the proposed control scheme.

KEYWORDS
actuator, attitude control, distributed multipole model, spherical motor, torque control, torque model

1 | INTRODUCTION

In recent years, various designs have been proposed for spherical motors with three-degree-of-freedom (3-DOF) rotation. Applications of 3-DOF spherical motors include simplified robot joints, omnidirectional mobility, and versatile actuators. However, the definition of 3-DOF movement has varied between different experimental realizations of this concept. For example, early designs of 3-DOF motors had a primary rotation axis, where the physical motor had an axle connected to the primary axis [1–4]. In these early models, 3-DOF rotation was defined as the ability to rotate the motor along the primary axis and the ability to tilt the orientation of the primary axis. Having a fixed primary axis simplifies control schemes by separating rotational motion from the tilting of the rotation axis.

Although this design is appropriate for certain applications, such as 3-DOF robot joints, it cannot be used in omnidirectional mobility applications requiring a full range of motion along an arbitrary axis. To construct spherical motors with a less limited range of motion, some researchers have designed motors in which the layout of the stator and rotor poles is nearly spherically symmetric. The earliest attempts at achieving a full range of motion in spherical motors were presented in papers on spherical stepping motors [5,6]. However, such motors do not support continuous rotation. Subsequently, control methods for similarly designed motors were refined to enable continuous rotation. Kasashima used a torque mapping method to perform open-loop control of continuous rotation [7]. However, at the time of publication, the exact orientation of the rotor could not be determined, meaning full closed-loop control of the motor was not possible.

Researchers working on spherical actuators were able to bypass this issue by using harmonic analysis of magnetic field distributions to implement torque control without prior knowledge regarding rotor orientation [8]. Previous

attempts at controlling 3-DOF motors have focused on obtaining an accurate orientation for the rotor and generating appropriate torque for the given rotor orientation. However, Rossini et al [8] used the magnetic field distribution of the rotor poles to calculate the required torques directly. The only drawback to their design is that it requires nine analog Hall sensors and the corresponding circuits to read and interpret analog signals in real time. For motors with more complex rotor pole geometries, as many as 24 single-axis Hall sensors are required [9].

It is evident from previous endeavors to realize a 3-DOF spherical motor that it is extremely difficult to provide an appropriate feedback signal for controlling the torque applied to the motor. To resolve this difficulty, we propose an alternate control method that only requires an approximate knowledge of the exact rotor orientation. In later sections, we detail this control method. Here, we note that the range of motion of our spherical motor design is somewhat limited because we constrain the rotational axis of the motor to lie within the equatorial plane of the motor, meaning the axis of rotation is free to rotate 360° within a plane, but not in a full 3D space. However, this limited range of motion is sufficient for omnidirectional mobility applications in which the motor is expected to drive spherical wheels on a flat, two-dimensional surface. Within these constraints, the simulation results we present demonstrate that the proposed control method is robust against small errors in rotor orientation estimation. Combined with the optical methods for determining rotor orientation that are referenced in previous works on spherical actuators [10,11], our control method is a feasible solution for driving a spherical motor.

In this paper, we present a design and torque model for a spherical motor that is suitable for continuous rotation along axes confined to the equatorial plane of a spherical wheel motor. The torque model is then used to develop a computationally efficient distributed multipole model, similar to the models presented in [12–15]. Using numerical methods, we demonstrate that it is possible to drive the motor with small rotational attitude error, even with limited knowledge regarding rotor orientation.

2 | MOTOR DESIGN

Our proposed spherical motor design consists of a ball-shaped rotor and a hemispherical stator shell with cylindrical air-core coils mounted on its outer surface. Previously, the rotor and stator pole layout of 3-DOF spherical motors had cylindrical symmetry to enable rotation along a primary axis. However, to enable rotation along an arbitrary axis, the stator coils must be positioned to maximize the spherical symmetry of the design. To find an arrangement of coils that maximizes spherical symmetry, researchers have examined regular polyhedrons, whose faces are identical regular polygons, as an inspiration for motor designs [5,6].

However, there is a finite number of ways to evenly arrange points on the surface of a sphere. The vertices of the five Platonic solids, which are examples of regular polyhedrons, are the only known instances. An icosahedron (Figure 1A) is one of the Platonic solids. It has 20 equilateral triangular faces and 12 vertices. We designed our stator by placing stator coils at the vertices of an icosahedron (labeled (v) in Figure 1A), as well as at the center of each triangular face (labeled (c) in Figure 1A). Mathematically, the vertices of an icosahedron can be described as permutations of (0, ±1, ±φ), where $\varphi = \left(1+\sqrt{5}\right)\Big/2$, as follows:

$$\text{icosahedron vertices} = \begin{cases} (0,\ \pm 1,\ \pm\varphi) \\ (\pm\varphi,\ 0,\ \pm 1) \\ (\pm 1,\ \pm\varphi,\ 0) \end{cases}. \tag{1}$$

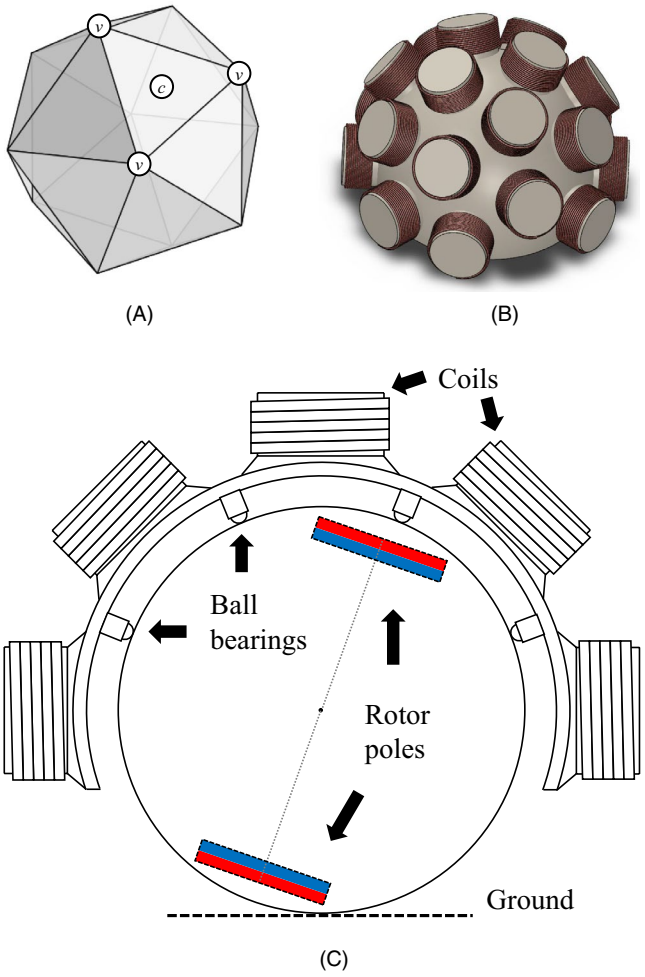

FIGURE 1 (A) Vertices (v) and center points (c) of an icosahedron. Coils are placed only on points that lie on or above the equatorial plane ($z = 0$). (B) An overview of the stator shell with circumferential stator coils. (C) A cross-sectional view of the spherical motor

An icosahedron has a total of 12 vertices. The center points (c) in Figure 1A can be calculated by averaging the three adjacent points of an icosahedron and normalizing its length to the norm of the vertices (v). To form a hemispherical stator shell, we selected the vertices of the icosahedron and the center points whose z components are greater than or equal to zero. Of the 12 vertices and 20 center points, only 20 points satisfy this requirement.

A schematic of the stator shell design is presented in Figure 1B, where each protrusion corresponds to a stator coil. A total of 20 stator coils corresponding to the 20 points chosen above were used in the proposed design. Figure 1C presents a cross-sectional view of the spherical wheel motor. We selected cylindrical rotor pole magnets that are magnetized along the cylindrical axis. They are located at the north and south poles of the rotor sphere. The stator shell is supported by ball bearings, which also keep the rotor sphere and stator shell concentric. In our current design, the rotor and stator shell are not connected directly. Instead, the stator shell rests on the rotor.

3 | PHYSICAL MODEL

3.1 | Torque model

The ball bearing support structure constrains the motion of the rotor sphere to keep it concentric with the stator shell. Therefore, the relative motion of the rotor sphere with respect to the stator shell is limited to rotational motion with no translational motion. Because the rotor poles and stator cores have cylindrical symmetry, the magnitude of the force between a single coil and rotor pole depends only on their separation angle (see Figure 2) and the coil current. In our analysis of the proposed motor, we focus solely on the forces acting on the rotor pole that is tangential to the rotor surface. The force component that is normal to the rotor sphere modifies the frictional forces acting on the ball bearings by changing the normal force acting on the bearings. In our numerical simulations, we ignore this effect for the analysis of our model. Therefore, the tangential component of the interaction force is defined as

$$\overrightarrow{F_i} = g\left(\theta_i\right) I_{\text{coil},i} \hat{\theta}_i, \tag{2}$$

where $I_{\text{coil},i}$ is the current through the i-th coil, $g(\theta_i)$ is the angular dependence of the force, and θ_i is the separation angle between the axes of the rotor pole and the i-th coil (see Figure 2A). The unit vector $\left(\hat{\theta}_i\right)$, which determines the direction of the interaction force, is defined as

$$\hat{\theta}_i = \begin{cases} \hat{r} \times \frac{(\hat{r}_i \times \hat{r})}{\|\hat{r}_i \times \hat{r}\|} & \left(\hat{r}_i \nparallel \hat{r}\right) \\ 0 & \left(\hat{r}_i \parallel \hat{r}\right) \end{cases}, \tag{3}$$

where $\hat{r}$ is the orientation of the rotor pole and $\hat{r}_i$ is the orientation of the i-th coil (see Figure 2B). As shown in (3), the unit vector $\hat{\theta}_i$ always points from the center of the magnet to the center of the i-th coil.

To obtain the angular dependence $g(\theta_i)$, we measure the back electromotive force (EMF) generated in the coil as a function of the separation angle and infer the generated torque from the back ENF measurement.

To explain the physical reasoning behind the method described above, we consider energy conservation in a motor. In a motor, power transferred to a coil is either exhausted as resistive coil loss or transferred to the motor as mechanical energy. Part of the transferred mechanical energy is converted into additional kinetic energy for the system and the remaining energy is lost as friction loss. This process can be written as follows:

$$\begin{aligned} P &= \text{coil loss} + \text{mechanical energy transfer} \\ &= (V - \varepsilon) I_{\text{coil}} + \varepsilon \times I_{\text{coil}}, \end{aligned}$$

where ε is the back EMF generated in the coil. The transferred mechanical energy is then converted into kinetic energy via the torque exerted by the stator coils. In a conventional motor, the generated torque is always parallel to the axis of rotation. However, in a spherical motor, the generated torque is not always parallel to the axis of rotation. While the parallel component of the torque adds to the kinetic energy, the perpendicular component causes precession of the rotational axis. Therefore, when analyzing the torque-power relationship in our spherical motor design, we only consider the parallel torque component. The parallel component of the torque is proportional to the mechanical power input and inversely proportional to the angular velocity, similar to the torque-power relationship of a conventional single-axis motor. Therefore, the instantaneous torque on the motor can be written as

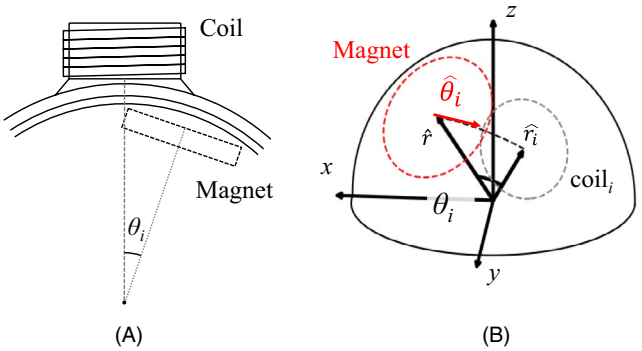

FIGURE 2 (A) Cross-sectional view of the rotor and a stator coil. (B) Definition of angles and vectors of the torque model

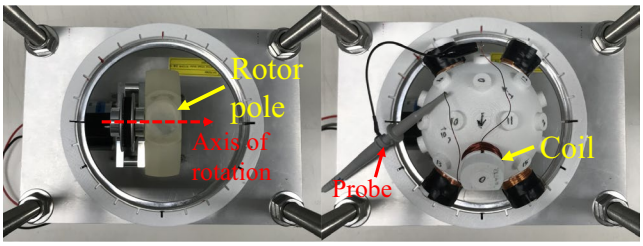

FIGURE 3 Back EMF measurement setup (A) without and (B) with the stator shell

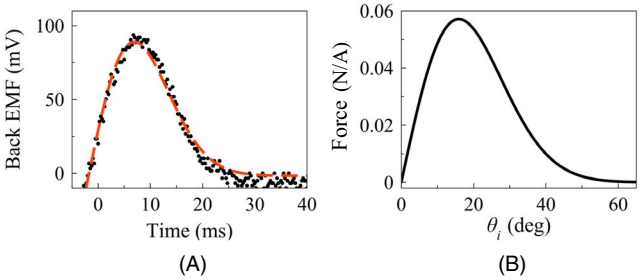

FIGURE 4 (A) Measured back EMF. (B) Angular dependence of the interaction force generated per unit current

$$\tau_{\parallel} = \frac{\varepsilon \times I_{\text{coil}}}{\omega}. \tag{4}$$

In summary, given the angular velocity and instantaneous back EMF, we can calculate the parallel component of the torque and the total torque generated by the coil. This empirical torque model can be used for further analysis of the motor.

To measure the back EMF generated in our design experimentally, we constructed an experimental setup in which we can measure the back EMF while driving the rotor at a constant speed using an external DC motor. Figure 3 presents the experimental setup used to measure the back EMF. For the purposes of measuring back EMF, we reduced the rotor shape to a spherical segment, which is a solid defined as a sphere cut by a pair of parallel planes. The resulting spherical segment was barely large enough to contain the rotor magnetic poles. The rotational axis of the modified rotor was connected to an axle and driven by an external DC motor at a constant velocity. The hemispherical stator shell was placed on top of the rotor (see Figure 3B). The rotor and stator coil were aligned such that when the rotor pole was beneath the stator coil, the central axes of the rotor pole and coil would be aligned. Two strands of AWG24 copper wire were wound for 100 turns to form the stator air-core coil. The stator core had a radius $r_{\text{coil}} = 1.5$ cm and length $l_{\text{coil}} = 1.5$ cm. For the rotor pole magnets, two cylindrical neodymium magnets with a radius $r_{\text{magnet}} = 1.5$ cm and length $l_{\text{magnet}} = 0.5$ cm were used.

In Figure 4A, we present the measured back EMF when the rotor is driven at a frequency of $f = 5$ Hz and an empirical fitting curve for the measured back EMF. By dividing the measured EMF by the observed angular speed (see (4)), we obtain the torque per unit current generated in a coil. In Figure 4B, we plotted the empirical fitting curve for the force as a function of the separation angle θ_i. The empirical torque model represented in Figure 4B is the following Gaussian derivative:

$$g\left(\theta_i\right) = g_0 \theta_i \exp\left(-\frac{\theta_i^2}{2\sigma^2}\right), \tag{5}$$

Where $g_0 = 17.2$ mN and $\sigma = 0.278$ rad (=15.9°).

3.2 | Mechanical model

Using the torque model defined above, we can construct a simple mechanical model for testing the dynamics of the spherical motor using numerical methods. When setting up the governing equations for motion, we made a simplifying assumption that the motor itself is not connected to any external load. This means that that the kinetic energy generated by the motor is stored only as the rotational kinetic energy of the spherical rotor wheel. We can then write the equations for motion as.

$$\frac{d\hat{x}}{dt} = \vec{\omega} \times \hat{x}, \tag{6}$$

$$\frac{d\vec{\omega}}{dt} = \frac{R}{I}\hat{x} \times \vec{F}_{\text{tot}} - \alpha\vec{\omega} - \vec{\beta}, \tag{7}$$

where $\hat{x}$ is the unit vector that indicates the orientation of the rotor dipole, $\vec{\omega}$ is the angular velocity, I is the moment of inertia of the rotor, R is the radius of the rotor, α is the velocity-dependent friction coefficient, and $\vec{F}_{\text{tot}}$ is the sum of all interaction forces between the coils and rotor, defined as follows:

$$\vec{F}_{\text{tot}} = \sum_{i}^{20} \vec{F}_i. \tag{8}$$

$\vec{\beta}$ is a friction term whose magnitude is constant and whose direction is chosen such that it always opposes motion as follows:

$$\vec{\beta} = \beta_0 \vec{\omega} / \left|\vec{\omega}\right|. \tag{9}$$

The frictional coefficients α and β_0 model the possible friction loss that can arise from the ball bearings supporting the structure. For our simulations, we used the parameter values listed in Table 1. By combining the equations for motion with the torque model, we can model the dynamics of the motor.

4 | CONTROL SCHEME

4.1 | Discretization of trajectory

The main challenge in controlling a spherical wheel motor is synchronizing the input to the stator coils to generate a desired torque [3,7]. Past attempts at torque control have demonstrated that it is possible to accomplish this synchronization under the conditions that (a) one has precise knowledge regarding the orientation of the rotor at all times or (b) the rotor orientation feedback mechanism samples frequently enough that any random errors in rotor orientation estimates can be averaged out. However, no practical methods have been developed that meet either of these requirements. To resolve this issue, we propose that the rotational trajectory be "discretized," meaning we define the trajectory as the path that the rotor pole follows during rotation. Instead of applying a different torque at every point along the rotational trajectory, we propose discretizing the trajectory into n segments and applying a constant set of coil inputs when the rotor passes through a given segment.

In a sense, the proposed control scheme only requires an approximate knowledge of the orientation of the rotor. We note that the trajectories that we are interested in are the largest circles that can be drawn on a sphere. Additionally, we focus on trajectories whose rotational axes lie on the xy plane, meaning they have zero z components ω_z of angular velocity. The z component of angular velocity does not contribute to the motion of a vehicle if a spherical motor is used for omnidirectional mobility. If the angular velocity of a rotor points solely in the z direction, the spherical wheel will simply rotate by itself while the vehicle connected to the motor remains stills. Each trajectory that satisfies the aforementioned constraint ($\omega_z = 0$) can be uniquely identified by its trajectory orientation ($\equiv\phi$), which we define as the azimuthal angle of the trajectory. It can also be defined as the angle between the angular velocity and x axis (see Figure 5).

To discretize trajectories, we divide the large circles into n evenly spaced segments. Figure 5 presents an example of trajectory discretization. For clarity, we only show the upper half of the trajectory. The alternating solid and dashed lines indicate the individual segments. To control the motor, we apply a constant input when the rotor orientation falls within a given segment. The set of inputs applied to the coil changes only when the rotor moves from one segment to the next segment.

4.2 | Current optimization method

To find the set of optimal currents using the *current optimization method*, we numerically simulate the motion of the rotor while varying the input current. However, it is uncertain which input should be applied to maintain the trajectory of the motor. The torque model gives us the forward function to compute the resulting position and angular velocity for a current input (h), but not for its inverse (h^{-1}), as shown below.

$$h: I_{\text{coil},i} \rightarrow \hat{x}(t), \vec{\omega}(t),$$

$$h^{-1}: \hat{x}(t), \vec{\omega}(t) \rightarrow I_{\text{coil},i}.$$

Therefore, to find the optimal set of current inputs, we numerically calculate the trajectory based on a set of coil currents, then attempt to minimize the deviation from the target trajectory by varying the input current.

In practice, we find the optimal input pulses by setting a constant target angular velocity ($\vec{\omega}_{\text{target}}$) and finding the input pulses required to maintain that angular velocity. To this end, we minimize the deviation of the angular velocity and rotor orientation from the target angular velocity and trajectory within a given segment. We quantify the deviation as

$$\text{loss} = \frac{1}{\Delta T}\int_0^{\Delta T} \left\|\vec{\omega}_{\text{target}} - \vec{\omega}(t)\right\|^2 + \left\|\hat{x}_{\text{target}}(t) - \hat{x}(t)\right\|^2 dt, \quad (10)$$

where ΔT is the time required to traverse a single segment. The target angular velocity and trajectory in (6) are defined as follows:

$$\vec{\omega}_{\text{target}} = \begin{cases} \omega_{\text{target}} \cos(\phi) \\ \omega_{\text{target}} \sin(\phi) \\ 0 \end{cases},$$

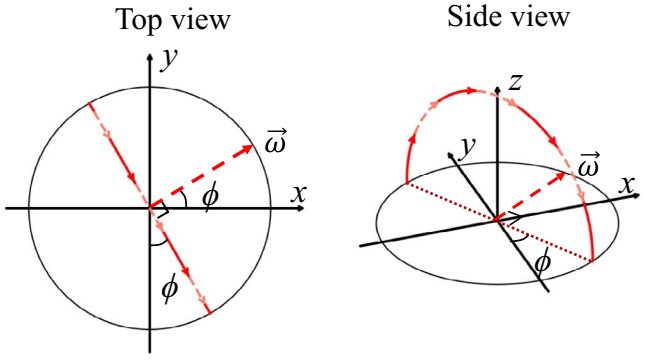

FIGURE 5 Diagram of discretized trajectory and trajectory orientation (ϕ). For clarity, only the upper half of the trajectory is shown

TABLE 1 Simulation parameters

Symbol	Quantity	Values
I	Moment of inertia	10^{-3} kg·m^2
R	Outer radius of rotor	0.05 m
α	Velocity-dependent friction coefficient	0.1 s^{-1}
β_0	Constant friction	10 rad·s^{-2}

$$\frac{\omega_{\text{target}}}{2\pi} = 1\text{Hz}.$$

$$\hat{x}_{\text{target}}(t) = \begin{cases} \sin(\phi)\sin(\omega_{\text{target}}t) \\ -\cos(\phi)\sin(\omega_{\text{target}}t) \\ \cos(\omega_{\text{target}}t) \end{cases},$$

In Figure 6, we visualize the result of such a simulation. In this numerical simulation, we attempted to calculate the current pulse required to maintain a trajectory with $\phi = 0°$. In Figure 6, we present currents flowing through selected coils during four consecutive trajectory segments. The red and blue arrows indicate the trajectories of the north and south poles of the rotor dipole, respectively. The direction of the current was chosen such that coils with positive current flow would attract the north pole of the rotor.

In Figure 6A, a large negative current through coil one pushes the rotor away while coils two and three pull the rotor with different strengths. The difference in the magnitude of the coil currents between coils two and three determines the trajectory orientation to correct for drifts in ϕ. In the subsequent steps, the coils push and pull the rotor to maintain the desired trajectory and angular velocity. The simulation results shown in Figure 6 were obtained by dividing the trajectory into $n = 20$ steps.

Although this current optimization method is too slow and impractical to be used for real motor control, it is a good way to test the feasibility of controlling a motor via discretization of trajectories. For example, this method can be used to find the minimum number of divisions required to drive a motor smoothly. While it is clear that smaller steps (larger n values) are better, the acceptable minimum number of steps is less clear.

In Figures 7A and 7B we present the angular velocity results obtained when we ran simulations with $n = 4$ and $n = 20$ divisions for a trajectory orientation of $\phi = 0°$. Divisions with $n = 4$ correspond to 90° steps, which are extremely coarse. Therefore, it is not surprising that a large angular velocity ripple is observed in the simulation results. When using finer steps ($n = 20$), we observed that the angular velocity ripple was significantly reduced (see Figure 7B).

We can quantify the angular velocity ripple by calculating the root-mean-square (RMS) deviation of the angular velocity as follows:

$$\Delta\omega_{\text{rms}} = \left[\frac{1}{T}\int_0^T \left\|\vec{\omega}_{\text{target}} - \vec{\omega}(t)\right\|^2 dt\right]^{1/2}, \quad (11)$$

where T is the period of rotation. A summary of the RMS deviation results obtained for different numbers of steps (n) is presented in Figure 7C. We observed that the angular frequency ripple reached an asymptotic limit at $n \geq 8$. In Figure 7D, we plot the RMS coil current, which is defined as

$$I_{\text{rms}} = \left[\frac{1}{mn}\sum_i^m \sum_j^n I_{\text{coil},i}^2\right]^{1/2}, \quad (12)$$

where n is the number of step divisions and m is the number of coils. One can see that as n increases, the RMS current pulse required to maintain the angular speed decreases, reaching an asymptotic limit at $n \sim 20$. We believe that if we use finer steps (larger n), we can transfer energy more efficiently to the rotor. However, the RMS current does not

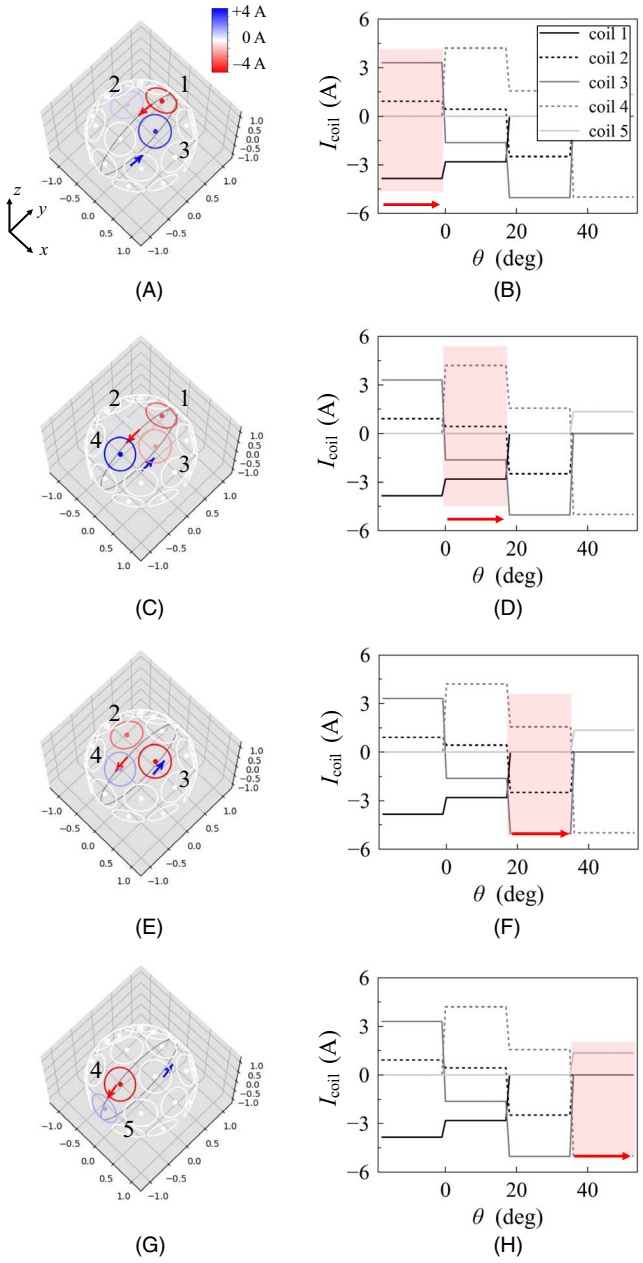

FIGURE 6 Simulation results for trajectories and optimal input currents for selected simulation segments. The red and blue colors of the coils in (A, C, E, G) indicate negative and positive currents, respectively. Red and blue arrows indicate the trajectories of the north and south poles of the rotor magnet, respectively

improve significantly beyond $n = 20$ because the stator coils are coarsely distributed over the stator shell surface.

To determine if it is possible to drive the motor along an arbitrary trajectory orientation, we carried out numerical simulations with various trajectory orientations ($\phi = 0°$, 15°, 30°, …, 90°) using $n = 20$ steps. We observed that although the angular velocity ripples are smaller for high-symmetry trajectories ($\phi = 0°$, 45°, 90°), the ripples are not excessively for intermediate angles (see Figure 7E). We also note that the RMS current required to drive the motor does not increase significantly for arbitrary trajectory orientations.

4.3 | Lookup table method

In the previous section, we demonstrated that it is theoretically possible to control the motor by discretizing trajectories and applying current inputs accordingly. However, the current optimization method involves a slow trial-and-error search for the optimal input currents. This process is not suitable for practical motor applications. In this section, we propose a realistic control scheme that is fast enough for use in an experimental setting. Instead of computing the optimal inputs at run time, we calculate them beforehand and control the motor by using the optimal values as lookup tables.

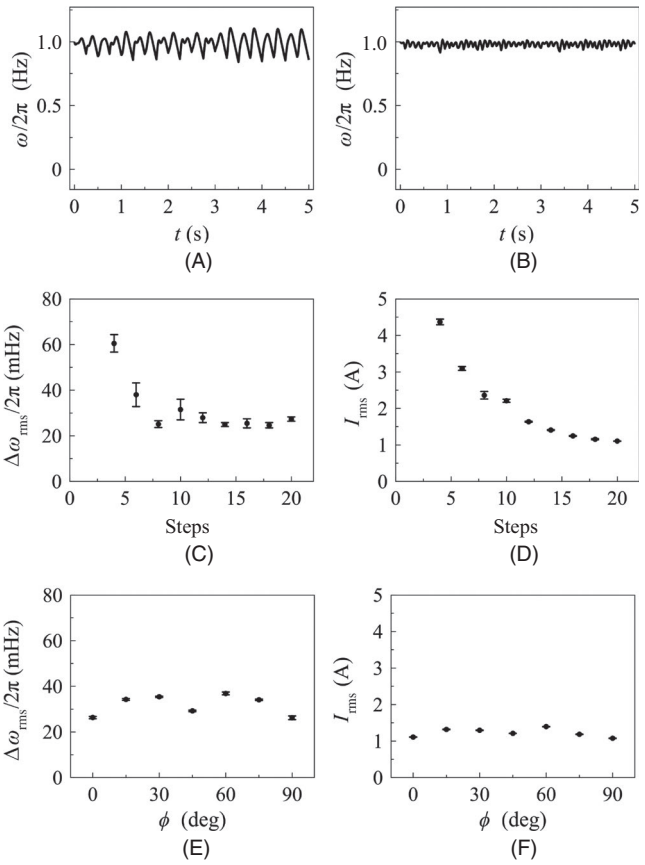

FIGURE 7 Rotational frequencies of simulated trajectories when they are discretized into (A) $n = 4$ and (B) $n = 20$ steps. (C) RMS deviation of rotational frequency from the target vs. discretization steps. (D) RMS average of input current vs. discretization steps. (E) RMS deviation of rotational frequency vs. trajectory orientation (ϕ). (F) RMS average of input current vs. trajectory orientation (ϕ)

In Figure 8, we present the control scheme diagram for the proposed lookup table method. The simulator takes an output polar angle (θ_{output}) as its input and passes a discretized polar angle (such as $\theta_{input} = 0°$, 30°, 60°, …) as an input for the lookup table. Depending on the target trajectory orientation (ϕ) and polar angle input, the lookup table outputs the pulse width modulation (PWM) duties to be used for the 20 individual coils. The PWM duties only change when the discretized polar angle (θ_{input}) changes.

In some respects, this is an incomplete control method because there is no explicit method for correcting for rotor attitude errors during run time. When we minimize the loss expression in (10), the current optimization method looks for current inputs that will correct rotor attitude errors if any are detected. However, when we use the lookup table method, we no longer detect rotational attitude errors because the motor only uses the polar angle (not the azimuthal angle) of the rotor position as a feedback signal. However, even without an explicit mechanism, we found that the motor trajectories remain relatively stable.

To simplify the simulation process and reduce the number of calculations, we assume that we can apply an arbitrary voltage input that ranges from 0 V to $V_{input} = 12$ V using the PWM method. In practice, this could be realized by using a fixed V_{input} for a multiphase inverter and applying different PWM duties to the inverters that control each coil. For this assumption to hold, the time constant of the coil must be much shorter than the duration of a single segment of a trajectory. Using $n = 20$ steps, a single segment lasts for longer than 10 ms when the motor is running at a frequency below 5 Hz. Therefore, the coil current can effectively charge up to the "equilibrium" current, which is estimated as $I_{equil} \sim V_{input} \times \text{PWM duty}/R_{coil}$. If we wish to model a motor operating at a frequency much faster than 5 Hz, we must account for the rise and fall of the coil current.

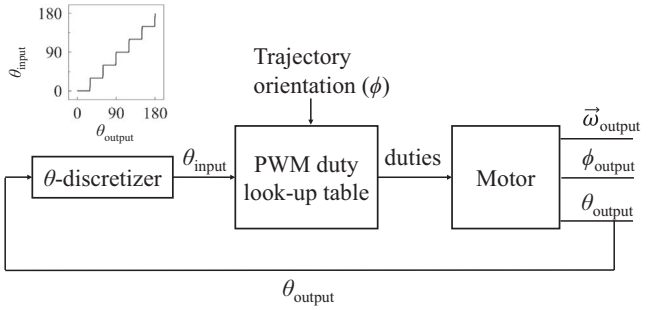

FIGURE 8 Main control scheme for the proposed lookup table method

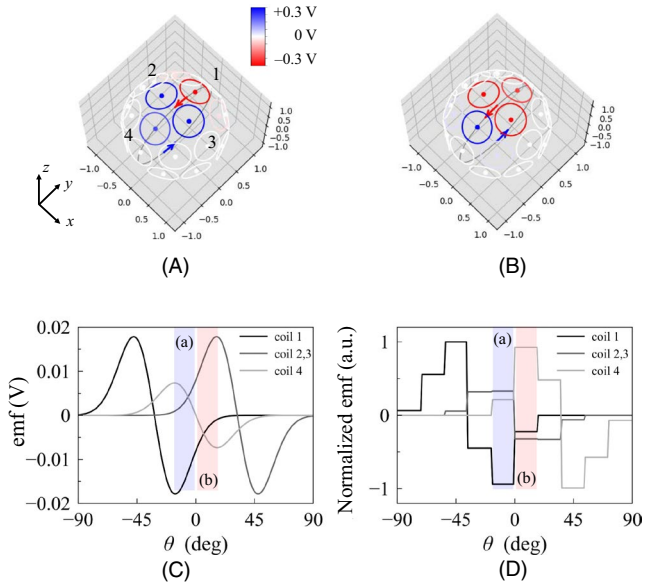

FIGURE 9 (A, B) Numerical simulation of trajectories and induced CV-EMF in the coils. Red and blue colors correspond to negative and positive back EMF, respectively. (C) Continuous CV-EMF in coils. (D) Discretized and normalized CV-EMF derived from the continuous CV-EMF. The blue and red shaded regions in (C, D) correspond to the trajectory segments shown in (A) and (B), respectively

To calculate the optimal PWM duties, we use two different methods. First, we calculate the optimal current pulses using the current optimization method for a given trajectory orientation ϕ. We obtain the optimal current pulses for five revolutions for a given ϕ and average the currents for each trajectory segment. The set of optimal currents is then normalized to the absolute maximum coil current observed during a single revolution. The normalized current pulses are then used as the PWM duties. We refer to this type of duty as a *current-based duty*. The positive and negative signs of the duties correspond to the coil current polarities.

For the second method, we numerically calculate the back EMF generated when the rotor is driven at a constant rotational frequency along a fixed trajectory orientation. To differentiate these values from the EMF induced in the coil during operation of the motor, we define these EMF values as constant-velocity EMF (CV-EMF). We then normalize the CV-EMF to the absolute maximum value of the CV-EMF and use the resulting values as PWM duties.

To obtain CV-EMF values, we simulated the rotation of a rotor along various trajectory orientations (ϕ = 0°, 15°, 30°, …). At each point along the trajectories, we numerically calculated the magnetic flux through each coil and used the numerical time derivatives of the flux values to obtain the induced EMF ($\varepsilon = -d\Phi/dt$).

Figures 9A and 9B present the trajectories and calculated CV-EMFs for selected coils. Figure 9C presents the numerically simulated back EMF for the coils labeled as one to four in Figure 9A and 9B. Because we wish to apply a constant PWM duty during a single segment, we average the CV-EMFs calculated over discrete segments. Figure 9C and 9D present the continuous CV-EMF, and discretized and normalized CV-EMF, respectively. The discretized and normalized EMF values were used as the PWM duty set. In the Appendix, we detail the physical reasoning for using these normalized CV-EMFs as PWM duty inputs. We refer to this set of duties as *EMF-based duties*.

By using the current-based and EMF-based duty sets, we numerically simulated the motion of the spherical motor. To quantitatively compare the outputs, the duties were normalized such that the power transferred to the coil per revolution when the rotor was rotating at the same frequency would be equivalent for each duty set.

$$\text{energy} \cong \frac{\sum_{i,j}^{20} \left(V_{\text{input}} \text{duty}_{ij}\right)^2}{R_{\text{coil}} \times \Delta T}, \tag{13}$$

where V_{input} is the input to the PWM module, duty_{ij} is the duty for i-th coil at the j-th step, R_{coil} is the resistance of a single coil, and ΔT is the time spent in a trajectory segment. In practice, normalizing the input energy is equivalent to normalizing the total sum of squares of duties over a single revolution.

In Figure 10A, we present the angular velocities obtained from numerical simulations of trajectories using EMF-based (solid line) and current-based (dashed line) duties. The

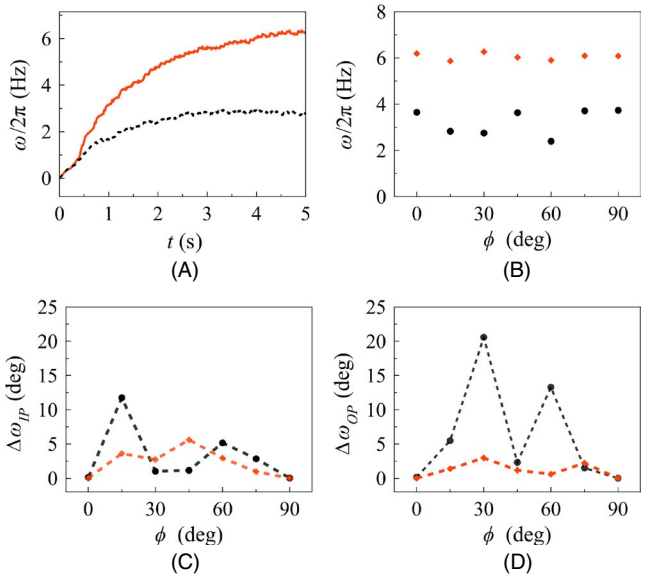

FIGURE 10 (A) Comparison of angular velocities obtained using EMF-based duties (red, solid line) and current-based duties (black, dashed line). (B) Terminal angular velocities for different trajectory orientations. (C) In-plane deviation from target trajectory orientations. (D) Out-of-plane deviation from target trajectory orientations. For (B–D), red symbols indicate EMF-based duty results and black symbols indicate current-based duty results

target trajectory orientation was set to $\phi = 30°$. One can see that although the input power per revolution is the same, the motor driven by EMF-duties achieves a higher terminal velocity. Because we have a velocity-dependent damping term in the governing equation (see (7)), this means that the average torque generated per revolution is higher when using EMF-based duties. In Figure 10B, we present the terminal velocities achieved for different trajectory orientations. One can see that the terminal velocity is consistently higher when using the EMF-based duty set. We also note that the terminal velocity does not vary significantly for different trajectory orientations, suggesting that the average torque applied by the motor does not change significantly when we change the target trajectory orientation.

However, as mentioned previously, the duty sets that we examined do not include any explicit methods for correcting a trajectory if the motor deviates from the intended trajectory. To quantify rotation attitude errors (deviations from a target trajectory), we examine the angle between the target angular velocity ($\vec{\omega}_{\text{target}}$) and terminal angular velocity ($\vec{\omega}_f$). In-plane and out-of-plane deviations are defined as

$$\Delta\omega_{\text{IP}} \equiv \cos^{-1}\left(\vec{\omega}_{t\,\text{arg}\,et} \cdot \vec{\omega}_{f,\text{IP}} \Big/ \left\|\vec{\omega}_{\text{target}}\right\| \left\|\vec{\omega}_{f,\text{IP}}\right\|\right), \quad (14)$$

$$\Delta\omega_{\text{OP}} \equiv \sin^{-1}\left(\frac{\omega_{f,z}}{\left\|\vec{\omega}_{f,\text{IP}}\right\|}\right), \quad (15)$$

where $\vec{\omega}_{f,\text{IP}} = \left(\omega_{f,x}, \omega_{f,y}, 0\right)$ is the in-plane component of the terminal velocity.

In Figure 10C, we present the in-plane deviations obtained from simulations using different duty schemes. One can see that the angular deviation is relatively small (<5°) when using EMF-based duties compared to using current-based duties. In Figure 10D, we present out-of-plane deviations. One can see that when using EMF-based duties, we can minimize the z component of the angular velocity, which does not contribute to the motion of a vehicle if the motor is used for omnidirectional motion.

5 | CONCLUSION

We examined a torque model for a novel motor design consisting of a magnetic dipole embedded in a spherical rotor with air-core coils placed on the hemispherical stator shell. Based on this torque model, we carried out numerical simulations of the motor dynamics and possible control schemes. We used current pulse optimization to demonstrate that discretizing the position information of the rotor can simplify motor control. We then compared the PWM duties obtained using the current optimization method to those derived from continuous-velocity back-EMF. Numerical simulations of closed-loop operation of the motor revealed that EMF-based duties can maintain a stable trajectory with minimal deviation from the target trajectory, even in the absence of an explicit mechanism for correcting deviations. The stability we observed during motor simulations using EMF-based duties demonstrates the feasibility of a simple method for controlling a spherical wheel motor with complex stator coil geometry.

To validate the performance and specifications of the proposed motor design, we must construct a physical prototype of the spherical motor and demonstrate closed-loop control. By measuring the attitude errors and how closely the velocity follows the control input, we should be able to validate the motor design.

ORCID

Junbo Park https://orcid.org/0000-0001-8039-0317
Hyun Gyu Jang https://orcid.org/0000-0003-3502-1613
Dong Yun Jung https://orcid.org/0000-0002-4793-7584

REFERENCES

1. K.M. Lee and C.K. Kwan, *Design Concept Development of a Spherical Stepper for Robotic Applications*, IEEE Trans. Robot. Autom. **7** (1991), no. 1, 175–181.
2. W. Wang et al., *Design and Control of a Novel Spherical Permanent Magnet Actuator with Three Degrees of Freedom*, IEEE/ASME Trans. Mechatronics **8** (2003), no. 4, 457–468.
3. K. Kahlen et al, *Torque control of a spherical machine with variable pole pitch*, IEEE Trans. Power Electron. **19** (2004), 1628–1634.
4. L. Yan et al, *Design and analysis of a permanent magnet spherical actuator*, IEEE/ASME Trans. Mechatronics **13** (2008), 239–248.
5. G.S. Chirikjian and D. Stein, *Kinematic Design and Commutation of a Spherical Stepper Motor*, IEEE/ASME Trans. Mechatronics **5** (1999), no. 4, 342–353.
6. T. Yano, *Proposal of Polyhedron Based Spherical Stepping Motors*, in SPEEDAM 2008 – Int. Symp. Power Electron. Electr. Drives, Autom. Motion, Ischia, Italy, June 11–13, 2008, pp. 1433–1438.
7. N. Kasashima et al., *Torque control method of an electromagnetic spherical motor using torque map*, IEEE/ASME Trans. Mechatronics **21** (2016), 2050–2060.
8. L. Rossini et al., *Closed-loop magnetic bearing and angular velocity control of a reaction sphere actuator*, Mechatronics **30** (2015), 214–224.
9. K. Bai and K.M. Lee, *Direct Field-feedback Control of a Ball-joint-like Permanent-magnet Spherical Motor*, IEEE/ASME Trans. Mechatronics **19** (2014), no. 3, 975–986.
10. D. Stein, E.R. Scheinerman, and G.S. Chirikjian, *Mathematical Models of Binary Spherical-motion Encoders*, IEEE/ASME Trans. Mechatronics **8** (2003), no. 2, 234–244.
11. M. Kumagai and R.L. Hollis, *Development of a Three-dimensional Ball Rotation Sensing System Using Optical Mouse Sensors*, in

Proc. – IEEE Int. Conf. Robot. Autom., Shanghai, China, May 9–13, 2011, pp. 5038–5043.
12. K.M. Lee and H. Son, *Distributed Multipole Model for Design of Permanent-magnet-based Actuators*, IEEE Trans. Magn. **43** (2007), no. 10, 3904–3913.
13. H. Son and K.M. Lee, *Distributed Multipole Models for Design and Control of PM Actuators and Sensors*, IEEE/ASME Trans. Mechatronics **13** (2008), no. 2, 228–238.
14. K.M. Lee, K. Bai, and J. Lim, *Dipole Models for Forward/inverse Torque Computation of a Spherical Motor*, IEEE/ASME Trans. Mechatronics **14** (2009), no. 1, 46–54.
15. H. Son and K.M. Lee, *Two-DOF Magnetic Orientation Sensor Using Distributed Multipole Models for Spherical Wheel Motor*, Mechatronics **21** (2011), no. 1, 156–165.

AUTHOR BIOGRAPHIES

Junbo Park received his BS degree in Physics from Harvey Mudd College in 2008. He received his PhD in applied physics from Cornell University, Ithaca, NY, USA in 2014. In 2015, he joined Electronics and Telecommunications Research Institute as a research scientist. His research interests include power electronics modules and power device fabrication. He is currently focused on studying SiC power devices and 3D motor design.

Minki Kim received his BS degree in Electrical Engineering and Computer Science from Kyungpook National University, Daegu, Rep. of Korea in 2008 and his MS degree in Electrical Engineering and Computer Science from Seoul National University, Rep. of Korea in 2010. Since 2010, he has worked at Electronics and Telecommunications Research Institute as a research engineer. His research interests include wide-band-gap power devices and power control systems.

Hyun Gyu Jang received his BS degree in Electronics Engineering from Korea Polytechnic University, Siheung, Rep. of Korea in 2013 and his MS degree in Advanced Device Technology from the University of Science, Rep. of Korea in 2015, where he studied gallium nitride power devices. In 2015, he joined the Electronics and Telecommunications Research Institute at Daejeon in the Republic of Korea as a Research Engineer. His current research interests include the design, fabrication, and characterization of electronic devices based on compound semiconductors, as well as the design of power supply units, such as inverters and converters.

Dong Yun Jung received his BS degree in Electronics and Materials Engineering (*first class honors*) from Kwangwoon University, Seoul, Rep. of Korea in 2001, and his MS degree and PhD *(excellence graduate)* in electrical engineering from the Korea Advanced Institute of Science and Technology, Daejeon, Rep. of Korea in 2003 and 2009, respectively. He has studied broadband integrated circuits for optical communications and low-power CMOS receiver circuits, as well as 3D modules using low temperature co-fired ceramic technologies for millimeter wave applications. He joined Electronics and Telecommunications Research Institute (ETRI) in the Republic of Korea in 2003 as an engineering researcher. From 2009 to 2014, he worked with the R&D Center of Samsung Electronics as a senior engineer, where he contributed to the development of millimeter wave integrated circuits. Since 2014, he has worked with ETRI as a principal researcher. His research interests include power electronics semiconductor devices and high-speed, high-efficiency power electronics conversion for high power and energy applications. He received the Best Paper Award from KAIST in 2007 and 2008. He also received a Silver Award in the SAMSUNG Best Paper Award competition in 2012.

Jong Moon Park received his BS degree in Electronic Engineering from Chonbuk National University, Rep. of Korea in 1982. He received his MS degree from the same university in 1991. He received a PhD in Semiconductor Science Technology from Chonbuk National University in 2010. Since 1985, he has worked at Electronics and Telecommunications Research Institute (ETRI), where he has been involved in semiconductor technology development of Si devices and lithography processes. He is currently the director of the Convergence Component Technology Center of ETRI. His research interests include silicon detectors and Si/SiC power device fabrication.

APPENDIX

In this section, we discuss the physical reasoning behind using CV-EMFs as duty values. In Figure A1, we present a decomposition of the force acting on the rotor pole as it passes by a stator coil in a straight line. There are two components to the interaction forces: parallel and perpendicular components. Parallel force increases or decreases the

rotational speed. Perpendicular force changes the direction of rotation and can introduce rotational attitude errors into the trajectory. If the straight path shown in Figure A1 is the desired trajectory, any perpendicular component in the interaction force can cause the rotor to deviate from the desired

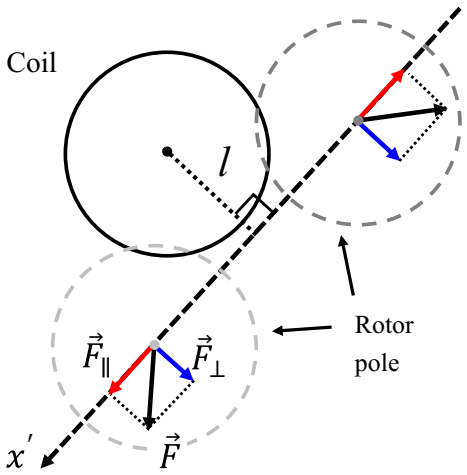

FIGURE A1 Decomposition of interaction force into components that are parallel (||) and perpendicular (⊥) to the trajectory. The black dashed line indicates the trajectory of the rotor pole

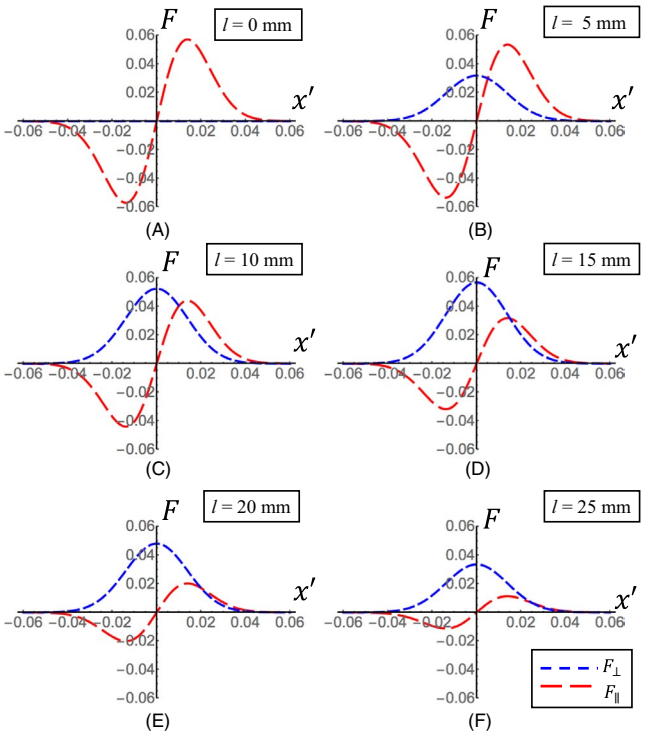

FIGURE A2 Parallel (red dashed lines) and perpendicular (blue dashed lines) components of interaction force vs the distance parameter x' (see Figure 11 for the definition of x')

path, meaning such forces should avoided be when possible.

In Figure A1, we present the interaction force as a function of the relative position of the rotor. We assume that a constant current is flowing through the coil. A distance parameter x' is also defined in Figure A1. The panels in Figure A2 reveal how the interaction force varies as we increase the separation distance l. The separation distance, as defined in Figure A1, is the shortest distance between the straight path and the center of the stator coil.

One can see that when $l = 0$, the rotor pole passes through the center of the coil and is not subjected to any perpendicular force. However, as the separation distance increases, the perpendicular component (blue dashed line) also increases. As expected, the perpendicular component of the force is maximized when the rotor is closest to the center of the magnetic pole, which corresponds to $x' = 0$ in the plots. It should be noted that the parallel force decelerates the rotor when $x' < 0$ and accelerates the rotor when $x' > 0$.

By modulating the coil current as a function of the relative position of the rotor x', we can minimize the perpendicular forces and maximize the parallel forces that accelerate the rotor. Because the parallel forces are antisymmetric about $x' = 0$ and the perpendicular forces are symmetric about $x' = 0$, we can apply a coil current that is antisymmetric about $x' = 0$. If we set the coil current at a given position x' to be proportional to the parallel force component shown in Figure A2, we get the modified set of forces shown in Figure A3.

There are three main points to consider regarding these new results. First, because the coil current is antisymmetric and zero at $x' = 0$, the peak perpendicular force is significantly reduced. Second, because the perpendicular force is antisymmetric about $x' = 0$, the perpendicular forces that cause rotational attitude errors average out as rotor poles pass by stator coils. Third, the parallel forces that are symmetric about $x' = 0$ consistently accelerate the rotor. Additionally, the shape and profile of the parallel component of the force shown in Figure A2 are proportional to the back EMF measured in each coil (see Figure A3). This is why it is physically practical to use CV-EMFs as duty profiles.

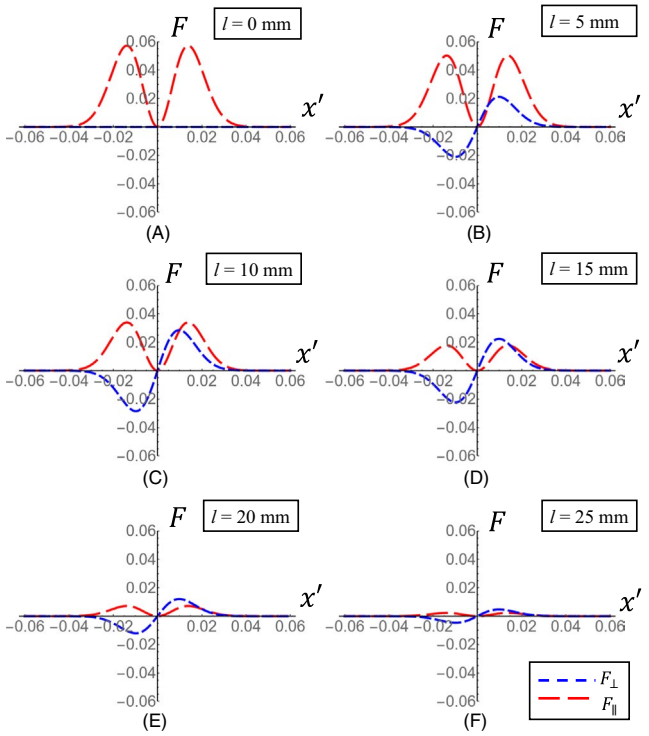

FIGURE A3 Parallel (red dashed lines) and perpendicular (blue dashed lines) components of interaction force multiplied by EMF duty. The modified force is plotted against the distance parameter x' (see Figure 11 for the definition of x')